

PAPER • OPEN ACCESS

Effect of oxygen contamination on densification of Fe(Se,Te)

To cite this article: A. Masi *et al* 2020 *J. Phys.: Conf. Ser.* **1559** 012051

View the [article online](#) for updates and enhancements.



IOP | ebooks™

Bringing together innovative digital publishing with leading authors from the global scientific community.

Start exploring the collection—download the first chapter of every title for free.

Effect of oxygen contamination on densification of Fe(Se,Te)

A. Masi^{1,2}, C. Alvani², A. Angrisani Armenio², M. Bellusci², G. Celentano², C. Fiamozzi Zignani², F. Fabbri², A. La Barbera², F. Padella², M. Pentimalli², E. Silva¹, A. Vannoizzi², F. Varsano²

¹ Università degli studi Roma Tre, Roma 00146, Italy

² ENEA, Roma 00196, Italy

andrea.masi@uniroma3.it

Abstract. The optimization of sintering behaviour of iron chalcogenides superconducting materials is mandatory to enhance their critical current density, in order to pursue their application in the production of superconducting wires. In this context it has been investigated here the effect of oxygen contamination on the material densification, considering the issues related to industrial oxygen-free isolated production lines. Our results show that the densification process is negatively affected by oxygen contamination. However, despite the difference in density, all sintered samples are characterized by similar structural and morphological features, and show comparable electrical and magnetic properties, with low critical current densities ($J_c < 10^3$ A/cm²). These results suggest that densification is not the key limiting factor in these conditions, and that grain boundary or misorientation factors may play a greater role in limiting the performance of sintered iron chalcogenides superconductors.

1. Introduction

Iron Based Superconductors (IBSCs) constitute a class of materials that, since their discovery [1], has attracted the attention of the scientific community for the intriguing coupling of magnetism and superconductivity. The scientific consideration is backed up by a significant applicative interest in the high-field magnet design sector. This interest is driven by the high critical magnetic fields and current densities characteristic of IBSC, making them a possible alternative to superconducting cuprates.

The IBSC materials share a common structural element, namely a layer composed by a square lattice of Fe in tetrahedral coordination with pnictides (P, As) or chalcogen (S, Se, Te) atoms. The different structures are then originated intercalating atoms, ions or molecules between the layers. Several families of iron based superconductors have been identified since the initial discovery, comprising the “1111” [1], the “122” [2] or the “11” [3] compounds, named after their stoichiometry. The research on the development of wires has started early since their discovery [4]. Despite the lower T_c of IBSCs with respect of cuprates, the IBSCs have several advantages in terms of lower anisotropy, higher symmetry of the superconducting phases and higher tolerance in grain boundaries. These factors allow to apply well developed and common processing routes already adopted to produce wires and tapes of alloy superconductors or MgB₂, such as the PIT method. Recent results obtained on iron pnictide superconductors demonstrate the high potential of these materials, with critical current density values that approach the target needed for application [5].

Iron chalcogenides, constituting the “11” family and exhibiting by the simplest crystalline structure among IBSC, are characterized by a significantly lower toxicity with respect to pnictide compounds.



Development of iron chalcogenides films has shown the potential of this family of materials, with high critical currents achieved at high fields [6]. The application of iron chalcogenides in superconducting wires has been however limited, hindered mostly by two factors: the high reactivity of the chalcogenides with the sheath metals [7] and the poor critical currents exhibited by consolidated polycrystalline materials [8][9]. Given the need to address the chemical compatibility issue, a deep understanding of the sintering behaviour of the powders and fine tuning of its texture is essential to improve densification and superconducting performance of the material.

This work is focused on the sintering behaviour of Fe(Se,Te) materials. In this framework, it is well known the affinity of iron chalcogenides for oxygen and therefore their reactivity with air and oxidizing agents [10], and the subsequent need to avoid any possible contamination. However, from the application perspective, oxygen-free isolated production lines are in contrast with large-scale production and reduction of costs. The effect of oxygen contamination on the sintering behaviour is therefore to be evaluated and considered. At the aim, densification of Fe(Se,Te) is here studied in relation to oxygen content. Crystalline structure and morphology of different sintered materials have been evaluated by means of X-Ray diffraction and microscopy techniques, assessing superconducting behaviour with electrical and magnetic measurements.

2. Experimental

Fe(Se,Te) powders were prepared through solid state reaction of Fe:Se:Te=1:0.5:0.5 at% (Fe from Sigma Aldrich, >99%, Se from Sigma Aldrich, 99.99% and Te from Sigma Aldrich, 99.8%) in a quartz vial under protecting atmosphere. The obtained powder was aged in air for different periods to achieve different oxygen contamination levels. The powder was then compressed in parallelepiped-shaped pellets with approximate dimensions $A \times B \times C \sim 8 \text{ mm} \times 3 \text{ mm} \times 1 \text{ mm}$. The so-prepared pellets (*green*) were subjected to a sintering treatment in a Thermal Programmed Desorption/Reduction (TPD/TPR) apparatus in Ar/H₂ atmosphere. The sintering thermal program was composed by a heating ramp up to 800 °C and 1 h of isothermal dwell. Two different heating rates were considered, 5 °C/min and 10 °C/min. The oxygen contamination was measured in situ via an indirect method, namely the evaluation of the amount of hydrogen consumed during the process.

Sintered density was evaluated by geometrical measurements. The reported uncertainty is estimated by statistical evaluation of several pellets sintered simultaneously. X-Ray Diffraction (XRD) analysis was carried out in a simultaneous 120 ° diffractometer (INEL PSD) equipped with a Fe K_{α1} radiation source. Morphological analysis was carried out by means of Polarized Light Optical Microscopy (PLOM) on polished sections to evaluate grain shape and size, and by means of a Leo 1525 Scanning Electron Microscope (SEM) to assess fracture morphology.

Superconducting characterization was carried out by means of electrical and magnetic measurements. Electrical resistance was measured using a standard four contacts method. Magnetic measurements were performed by means of an Oxford Instrument Vibrating Sample Magnetometer (VSM) on the same samples. Measurements were carried out with the field applied parallel to the C sample axis. Direct Current (DC) magnetization was measured in Zero Field Cooling (ZFC) and Field Cooling (FC) conditions applying a 0.002 T magnetic field.

3. Results and discussion

The theoretical volumetric mass density of the compound was estimated as 6.2 g/cm³, considering the structure and lattice parameters reported in literature for Fe(Se,Te) [11]. The green density of the pressed samples was measured as approximately 82% of the theoretical density.

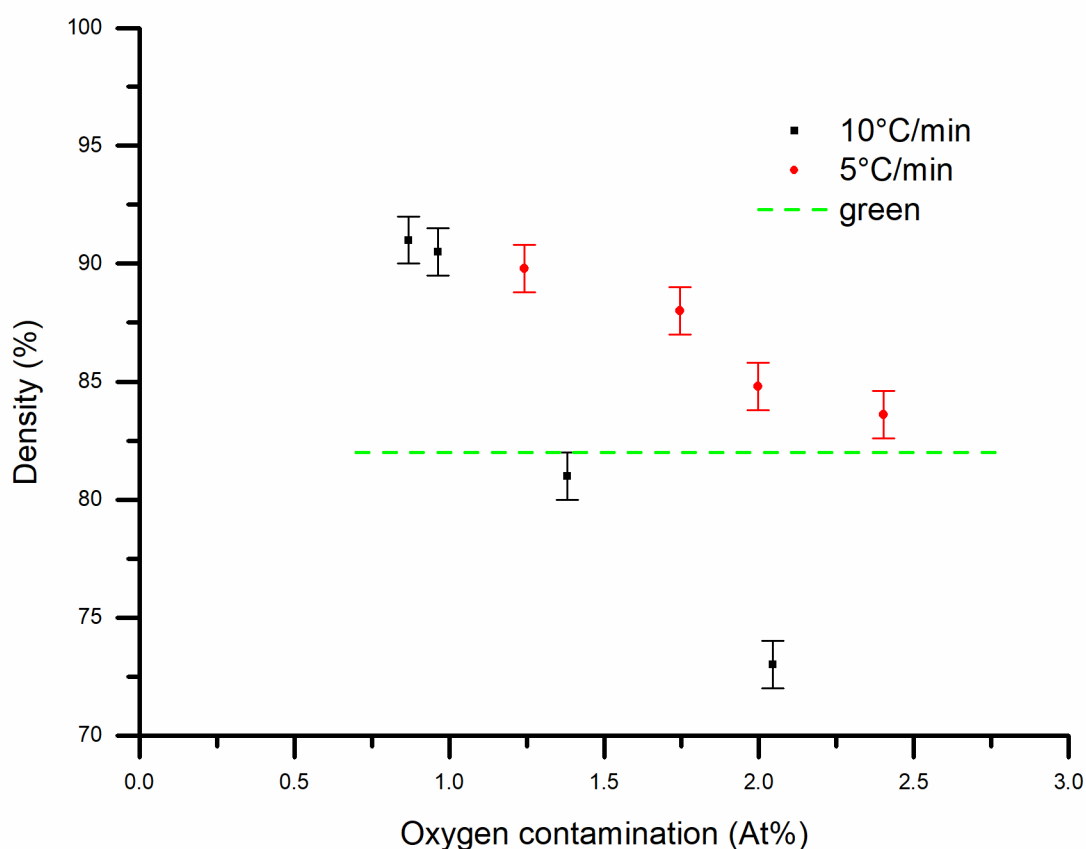


Figure 1. Volumetric mass density as a function of oxygen contamination for the different heating rates.

In Figure 1 the results of the sintering experiments are reported as a function of the oxygen contamination measured for each set of samples. Samples characterized by low oxygen content reach density of approx. 90%. For increased oxygen content a decrease of sintering density is evident for both different sintering heating rate. These results suggest that oxygen tend to accumulate at grain boundaries, acting as an inhibitor during the densification process.

The swelling observed for some of the samples may be due to the development of porosity following the formation and entrapment of gaseous species, such as Se and Te - given their high vapour pressure [12]. The difference among the two heating ramps shows how this phenomenon is mitigated for lower heating rates. A fast heating process may in fact lead to pore closing with high volumes of trapped gas, with a consequent inhibition on the material densification. The lower heating rate is expected to delay the pore-closing phase, leaving more time for the developing gas to be released and therefore allowing for a more effective sintering.

XRD patterns of the starting powder and of several samples characterized by different densities are reported in Figure 2. All patterns exhibit a tetragonal $P4mm$ $Fe(Se,Te)$ phase as main constituent, with minor peaks ascribable to an hexagonal-like (e.g. δ - $FeSe$ or Fe_7Se_8) secondary phase. For the sintered samples, a high angle broadening of tetragonal phase peaks, particularly evident for the $00l$ peaks, suggests the presence of multiple chemically inhomogeneous tetragonal phases, as widely reported for $Fe(Se,Te)$ materials [13–16]. No significant difference can be observed between sintered samples characterized by different densities.

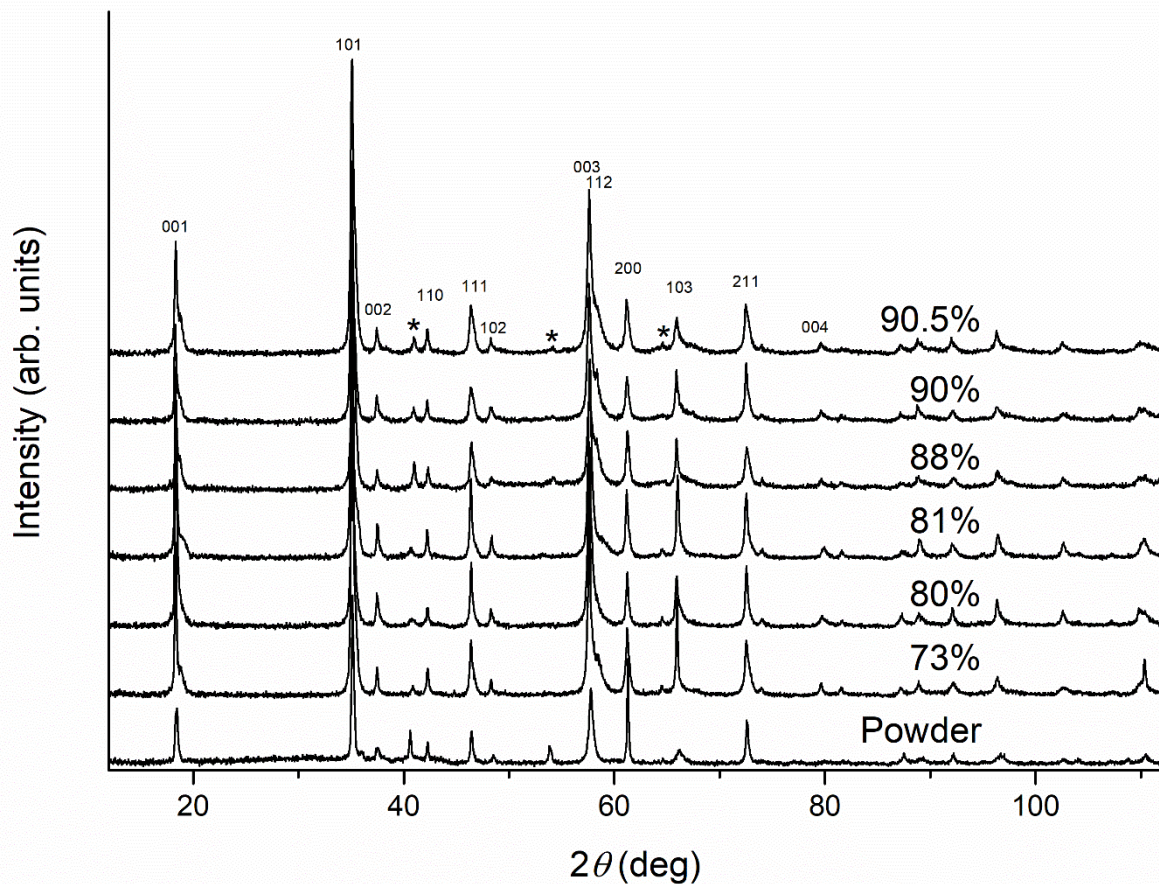


Figure 2. XRD patterns of the initial powder and of samples characterized by different final density. Peaks ascribed to the P4mm Fe(Se,te) tetragonal phase are labelled, while * indicates peaks ascribable to the hexagonal-like secondary phase.

The electrical resistance was measured for the different samples. No significant differences were observed in different samples apart from the absolute value of resistivity, that decreased with density starting from approx. $1.5 \text{ m}\Omega\cdot\text{cm}$ for the less dense 73 % sample and reaching approx. $1 \text{ m}\Omega\cdot\text{cm}$ for the denser 90 % samples. The curve shape was similar for all the sintered samples: in Figure 3 is reported the curve measured for a 90% sample.

The curve shows a semi-conducting behaviour above approx. 200 K, while below this value the resistivity tends to decrease when lowering the temperature. At low temperature, a superconducting transition is observed, starting at approx. 15 K, with the resistance vanishing at approx. 12 K.

All sintered samples were characterized by similar critical temperature, with values comprised between 14 K and 15 K, and by broad transitions, with $\Delta T_c^{90\%-1\%}$ values in the 2 K – 4 K range, without a clear influence of final density.

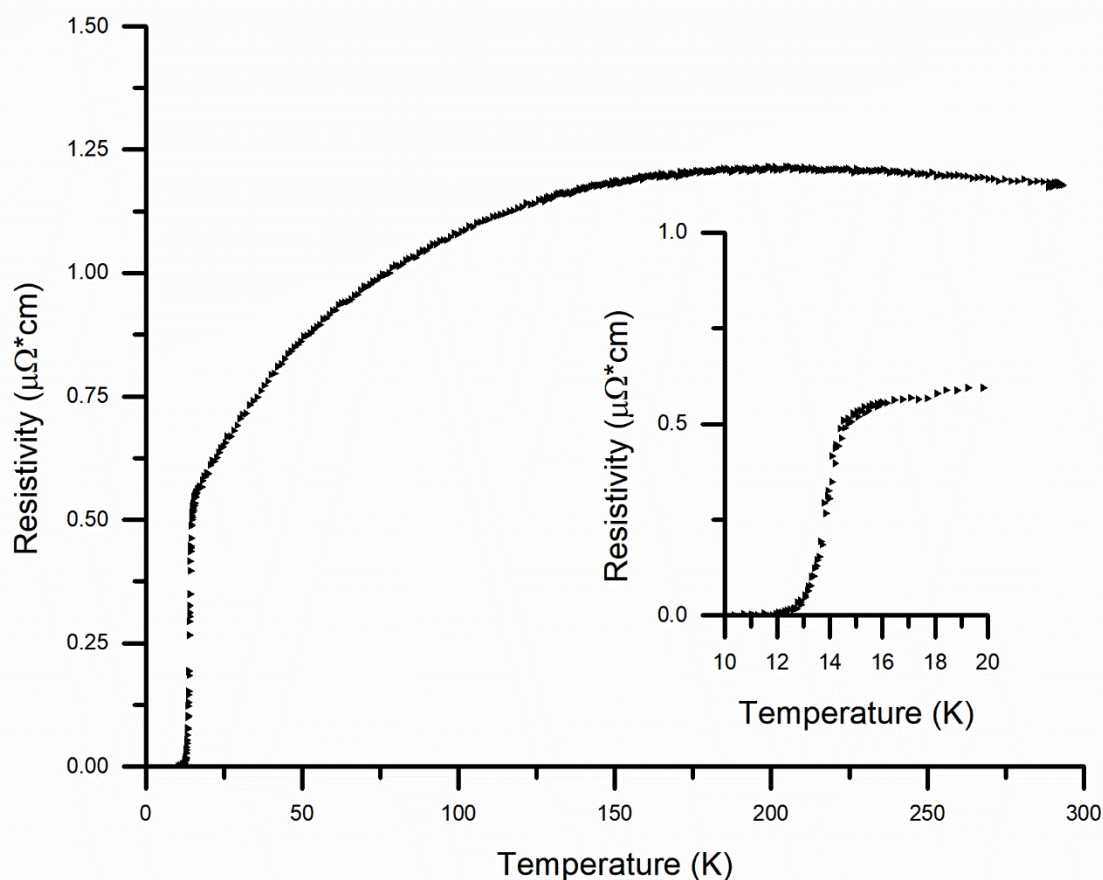


Figure 3. Electrical resistivity as a function of temperature for a 90% density sintered sample (see text for details); in inset, detail of the superconducting transition.

Regarding the transition width, it is worth to be noted that Fe(Se,Te) polycrystalline samples are often characterized by broad superconducting transitions, that may be due to several factors such as chemical homogeneity or mechanical stress [17]. However, as evident in our work and previously reported in literature (e.g. [9,18,19]), broad transitions in sintered samples are mostly due to the presence of low temperature resistive tails. This may suggest the occurrence of weak-link phenomena, likely ascribable to insulating grain boundaries or to misalignment issues.

To gather a deeper insight on this aspect, a thorough evaluation of the morphology of samples characterized respectively by low and high density was carried out by means of microscopy analyses, and the results are reported in Figure 4 and Figure 5.

The samples fracture analysis by means of SEM highlights how the sintered samples are formed by highly crystalline aggregates of platelet-like grains randomly oriented. The significantly different density difference – 73% vs 90% in the comparison – is not revealed by SEM, and no significant differences among the samples are evident.

PLOM analysis, performed on polished sections of the same two samples clearly highlights instead the different porosity. The sample characterized by 73% final density is characterized by the diffuse presence of large irregular pores, with diameter in the tens - hundreds of μm range. On the contrary, as expected, porosity presence is substantially lower in the 90% dense sample. Observing at higher magnification, the crystalline morphology is clear: both samples are characterized by the presence of equiaxed grains of similar size, with an average diameter of $17 \pm 5 \mu\text{m}$ and $16 \pm 4 \mu\text{m}$ respectively for the 73% and 90% sample.

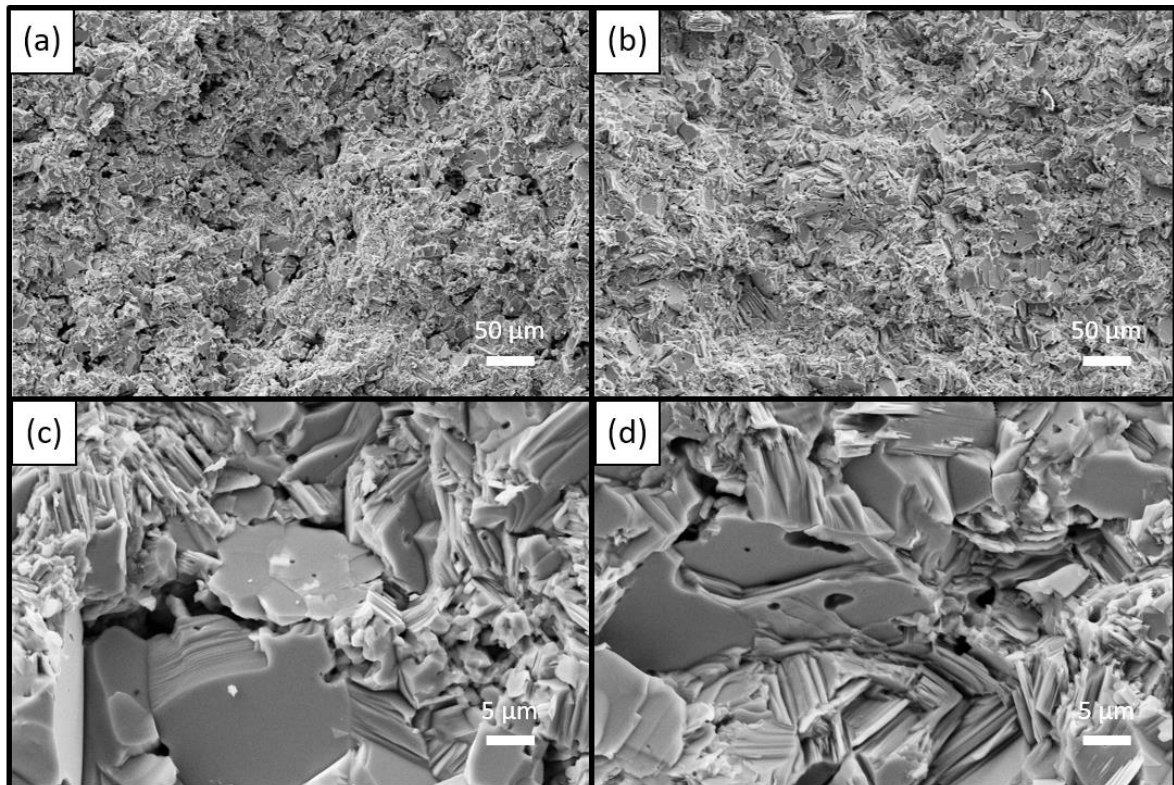


Figure 4. SEM images of fractures of samples characterized by 73% (a,c) and 90% (b,d) density.

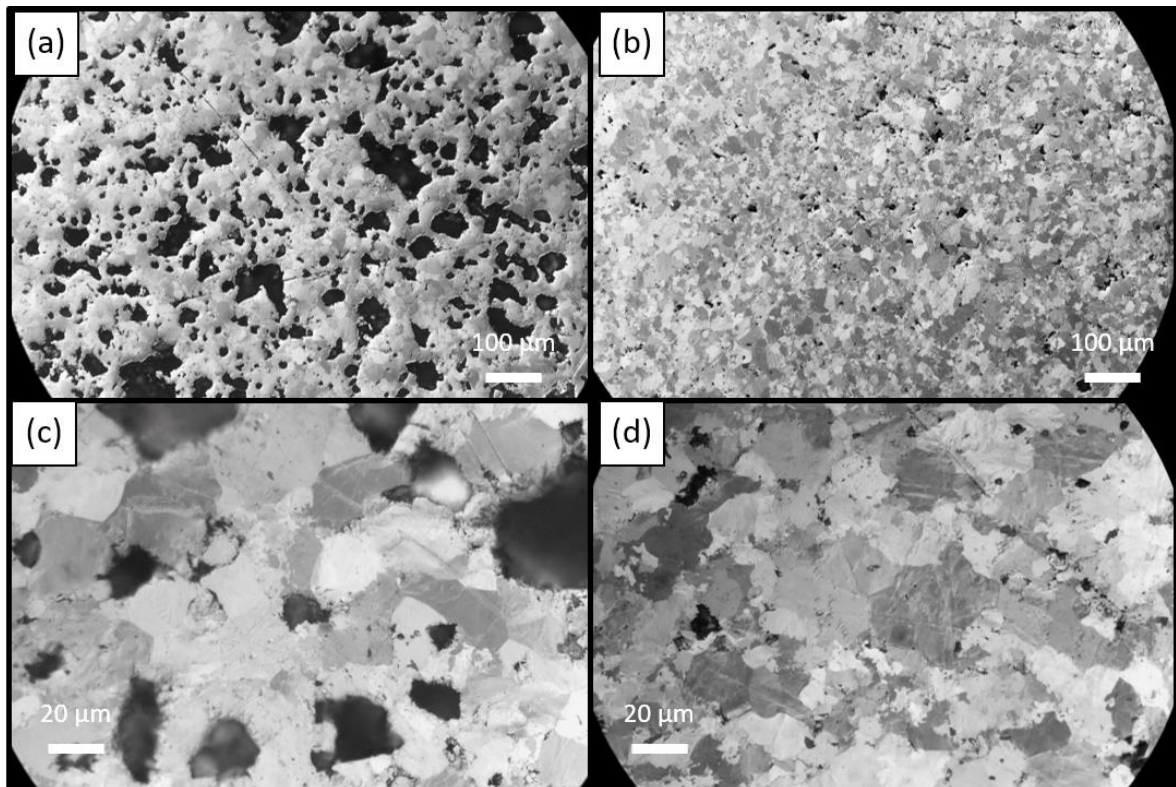


Figure 5. POM images of polished sections of samples characterized by 73% (a,c) and 90% (b,d) density.

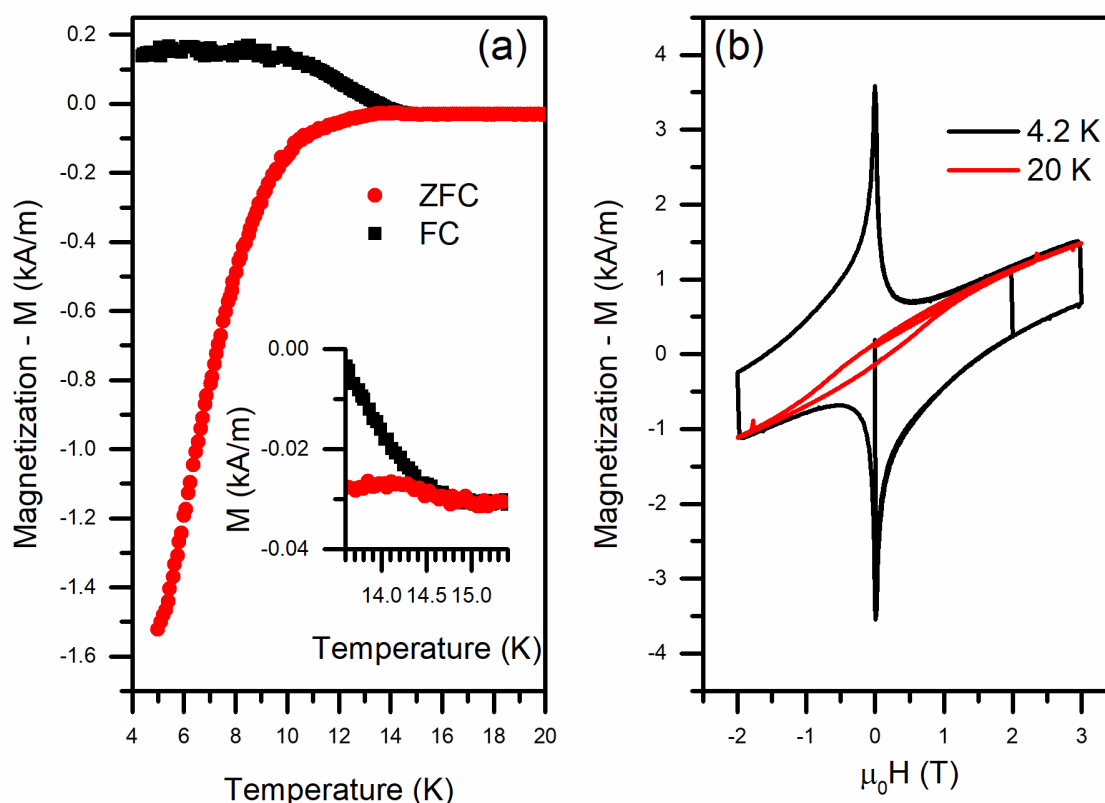


Figure 6. Magnetic characterization of a 90% density sintered sample: (a) ZFC and FC curves as a function of temperature, with details of the transition in inset; (b) magnetic hysteresis loops at 4.2 K and 20 K.

In Figure 6 the results of the magnetic characterization of a 90 % density sintered pellet are reported. Figure 6(a) shows ZFC and FC curves as a function of temperature: the compound is characterized by a broad superconducting transition, with onset slightly above 14 K. The magnetic hysteresis loops acquired at 4.2 K and 20 K are reported in Figure 6(b). At low temperature, a superconducting loop can be observed, with evidence of the presence of other non-superconducting magnetic phases, compatibly with the XRD peaks ascribable to the hexagonal-like secondary phase [20]. The hysteresis loop measured at 20 K highlights this evidence, with an open hysteresis ascribable to a ferro/ferrimagnetic phase.

In our experiments, the magnetic properties of the sintered samples did not show significant dependence on their density. Considering the similarity of structural, morphological and electrical characteristics, this result suggests that the bulk superconducting properties as well is not influenced - at this level - by the final density. It is worth to be noted, however, that the hysteresis magnitude is not comparable with single crystals or polycrystalline samples obtained by means of melting techniques [16]. The magnetic results obtained on our sintered samples are instead comparable with results previously reported in literature for similar non-melted samples [18], with broad transitions and narrow hysteresis loops. An estimation of the critical current density by means of the Bean's model results in values lower than 10^3 A/cm² in self field, two orders of magnitude lower with respect to values obtained in single crystals and films. This may be related to grain boundary limiting effects and to misorientation factors, suggesting that in sintered samples, despite the presence of Fe(Se,Te) superconducting phases characterized by high T_c , a relatively good overall density is not sufficient to obtain high J_c .

4. Conclusions

In this work, the role of oxygen contamination in the sintering process of Fe(Se,Te) materials was evaluated and assessed. Several samples were obtained using powders characterized by different oxygen contamination. The green samples were subjected to a sintering treatment at 800 °C, adopting two different heating rates. Our results show that sintered density is clearly dependent on oxygen content, that affects negatively the sintering process. Slower heating rates lead to higher sintering density, possibly due to a mitigated tendency of trapping gases that evolve during the process.

The obtained samples, ranging from 73 % to 90 % density, are characterized by similar structural and morphological features, and show comparable electrical and magnetic properties, with the presence of superconducting phases with $T_c \sim 14$ K. The low measured critical current density ($J_c < 10^3$ A/cm²) suggests that density is not the key limiting factor. Grain boundary or misorientation factors are expected therefore play a key role in the enhancement of high-field performance of sintered iron chalcogenides superconductors.

References

- [1] Kamihara Y, Watanabe T, Hirano M and Hosono H 2008 Iron-based layered superconductor La[O_{1-x}F_x]FeAs ($x = 0.05-0.12$) with $T_c = 26$ K *J. Am. Chem. Soc.* **130** 3296–7
- [2] Rotter M, Tegel M and Johrendt D 2008 Superconductivity at 38 K in the iron arsenide (Ba_{1-x}K_x)Fe₂As₂ *Phys. Rev. Lett.* **101** 4–7
- [3] Hsu F-C, Luo J-Y, Yeh K-W, Chen T-K, Huang T-W, Wu P M, Lee Y-C, Huang Y-L, Chu Y-Y, Yan D-C and Wu M-K 2008 Superconductivity in the PbO-type structure α -FeSe *Proc. Nat. Acad. Sci. USA* **105** 14262–4
- [4] Hosono H, Tanabe K, Takayama-Muromachi E, Kageyama H, Yamanaka S, Kumakura H, Nohara M, Hiramatsu H and Fujitsu S 2015 Exploration of new superconductors and functional materials, and fabrication of superconducting tapes and wires of iron pnictides *Sci. Technol. Adv. Mater.* **16** 033503
- [5] Hosono H, Yamamoto A, Hiramatsu H and Ma Y 2018 Recent advances in iron-based superconductors toward applications *Mater. Today* **21** 278–302
- [6] Si W, Han S J, Shi X, Ehrlich S N, Jaroszynski J, Goyal A and Li Q 2013 High current superconductivity in FeSe_{0.5}Te_{0.5}-coated conductors at 30 tesla *Nat. Commun.* **4** 1347
- [7] Palombo M, Malagoli A, Pani M, Bernini C, Manfrinetti P, Palenzona A and Putti M 2015 Exploring the feasibility of Fe(Se,Te) conductors by ex-situ powder-in-tube method *J. Appl. Phys.* **117** 1–9
- [8] Ding Q, Taen T, Mohan S, Nakajima Y and Tamegai T 2011 Magneto-optical imaging of polycrystalline FeTe_{1-x}Se_x prepared at various conditions *Phys. C Supercond.* **471** 651–5
- [9] Ding Q, Mohan S, Tsuchiya Y, Taen T, Nakajima Y and Tamegai T 2011 Low-temperature synthesis of FeTe_{0.5}Se_{0.5} polycrystals with a high transport critical current density *Supercond. Sci. Technol.* **24** 075025
- [10] Sun Y, Taen T, Tsuchiya Y, Shi Z X and Tamegai T 2013 Effects of annealing, acid and alcoholic beverages on Fe_{1+y}Te_{0.6}Se_{0.4} *Supercond. Sci. Technol.* **26** 015015
- [11] Yeh K-W, Huang T-W, Huang Y-L, Chen T-K, Hsu F-C, M. Wu P, Lee Y-C, Chu Y-Y, Chen C-L, Luo J-Y, Yan D-C and Wu M-K 2008 Tellurium substitution effect on superconductivity of the α -phase iron selenide *EPL (Europhysics Lett.)* **84** 37002
- [12] Brooks L S 1952 The Vapor Pressures of Tellurium and Selenium *J. Am. Chem. Soc.* **74** 227–9
- [13] Bhatia V, Rodriguez E E, Butch N P, Paglione J and Green M a 2011 Phase separation and superconductivity in Fe_{1+x}Te_{0.5}Se_{0.5} *Chem. Commun.* **47** 11297
- [14] Sala A, Palenzona A, Bernini C, Caglieri F, Cimberle M R, Ferdeghini C, Lamura G, Martinelli A, Pani M, Hecher J, Eisterer M and Putti M 2014 Evidence of a miscibility gap in the FeTe_{1-x}Se_x polycrystalline samples prepared with a melting process *J. Phys. Conf. Ser.* **507** 012044
- [15] Masi A, Alvani C, Augieri A, Bellusci M, Celentano G, De Marzi G, Fabbri F, Zignani C F,

- La Barbera A, Padella F, Pentimalli M, Silva E, Vannozzi A and Varsano F 2018 Phase Separation and Microstructure in Superconducting FeSe_{1-x}Te_x Materials *IEEE Trans. Appl. Supercond.* **28** 7300305
- [16] Masi A, Alvani C, Augieri A, Bellusci M, Celentano G, De Marzi G, Fabbri F, Fiamozzi Zignani C, La Barbera A, Padella F, Pentimalli M, Silva E, Vannozzi A and Varsano F 2019 Fe(Se,Te) From Melting Routes: Insight on Phase Separation *IEEE Trans. Appl. Supercond.* **29** 7300304
- [17] Martinelli A, Bernardini F and Massidda S 2016 The phase diagrams of iron-based superconductors: Theory and experiments *Comptes Rendus Phys.* **17** 5–35
- [18] Awana V P S, Pal A, Vajpayee A, Mudgel M, Kishan H, Husain M, Zeng R, Yu S, Guo Y F, Shi Y G, Yamaura K and Takayama-Muromachi E 2010 Synthesis and physical properties of FeSe_[sub 1/2]Te_[sub 1/2] superconductor *J. Appl. Phys.* **107** 09E128
- [19] Chen N, Liu Y, Ma Z, Yu L and Li H 2016 Improvement in structure and superconductivity of bulk FeSe_{0.5}Te_{0.5} superconductors by optimizing sintering temperature *Scr. Mater.* **112** 152–5
- [20] Terzieff P and Komarek K L 1978 The Antiferromagnetic and Ferrimagnetic Properties of Iron Selenides With NiAs-Type Structure *Monatshefte* **1047** 1037–47